FE thermo-mechanical simulation of welding residual stresses and distortion in Ti-containing TWIP steel through GTAW process

V. García-García[a,b], I. Mejía[a,*], F. Reyes-Calderón[b], J.A. Benito[c], J.M. Cabrera[a,c]

[a] Instituto de Investigación en Metalurgia y Materiales, Universidad Michoacana de San Nicolás de Hidalgo, Edificio "U-3", Ciudad Universitaria, 58030-Morelia, Michoacán, México.

[b] Departamento de Metal Mecánica, Posgrado en Metalurgia / Doctorado en Ciencias en Ingeniería. Tecnológico Nacional de México / Instituto Tecnológico de Morelia, Av. Tecnológico 1500, 58120-Morelia, Michoacán, México.

[c] Departamento de Ciencia e Ingeniería de Materiales, EEBE, Universitat Politécnica de Catalunya, c/Eduard Maristany 10-14, 08019-Barcelona, Spain.

* Corresponding author. Tel.: +52 (443) 322 3500 Ext: 4009; Fax: +52 (443) 322 3500 Ext: 4010. E-mail address: imejia@umich.mx, i.mejia.granados@gmail.com

Abstract

The effect of residual stresses can be beneficial or harmful depending on their magnitude, type and distribution. This research work applied the isotropic and kinematic hardening models with different strain rates (0.001-100 s^{-1}) to simulate the non-linear mechanical behavior of Twining Induced Plasticity (TWIP) steel microalloyed with titanium. A finite element (FE) thermo-mechanical model was employed to analyze the welding thermal cycle in the TWIP-Ti steel. The numerical prediction of residual stress was validated by X-ray diffraction (XRD) measurements in welding critical regions. Furthermore, a residual stress critical zone (SCZ) was defined as a function of the maximum tensile residual stress and hardness in the fusion zone (FZ) and heat affected zone (HAZ). The magnitude of residual stresses estimated in the SCZ was lower than TWIP-Ti steel yield strength. The weld joint preparation and the mechanical constraint provided a control to mitigate both residual stress and distortion. Quantitatively, the results provided good weldability of the TWIP-Ti steel in higher plate thickness through the Gas Tungsten Arc Welding (GTAW) process at low heat input.

Keywords: TWIP-Ti steel; welding; finite element simulation; residual stress; hardening model; X-ray diffraction.

1. Introduction

High-Mn austenitic steels exhibiting twining induced plasticity (TWIP) effect have attracted a growing interest for the automotive industry **[1]**. TWIP steels offer high strength and ductility as well as relatively high impact energy absorption, which are desirable properties in automotive structural design **[2]**. Another requirement in the latter industry is the weldability of the new steels introduced. This is particularly true in TWIP steels where weldability studies are infrequent. Indeed current interest in welding application of TWIP steels is focused on welds in low thickness plates (1-3 mm) obtained through the resistance spot welding (RSW) **[2-3]** and laser beam welding (LBW) **[4-5]** processes.

A major welding problem is the presence of residual stresses and distortion due to the localized heat input, which generates a non-uniform deformation distribution **[6]**. Residual stresses produced in the weld bead region and adjacent zones are deleterious because they can promote brittle fracture, fatigue strength reduction as well as hot and corrosion cracking propagation **[7-8]**.

It is also well-known that heat input has a direct relationship with the magnitude of both residual stresses and distortion in welding **[9]**. Particularly, TWIP steels are high sensitive to welding heat input which affects both microstructure and mechanical properties **[1, 10]**. Grain growth in the heat affected zone (HAZ) and mechanical strength reduction generate favorable conditions for hot cracking in both fusion zone (FZ) and HAZ, which is a typical defect that limits TWIP steel weldability **[2, 11]**. In consequence, the study of the mechanical field around the welding area is important to establish a relationship between residual stresses and structural integrity in the FZ and HAZ of TWIP steel.

However, the literature related to measurement or prediction of residual stress during welding operations in TWIP steel as well as its plastic deformation behavior during the thermal cycle, is scarce. Previous research works so far have been carried out by Mujica et al. **[12]** and Colombo et al. **[13]**. They measured residual stresses in a dissimilar weld TWIP-TRIP steels and a resistance-spot weld of Fe-16.4Mn-0.75C-1.9Al TWIP steel sheets, respectively, using X-ray diffraction.

Other research works have studied the mechanical behavior of TWIP steels. For instance, Shterner et al. **[14]** proposed a constitutive model for a Fe-18%Mn-0.6%C-1%Al TWIP steel based on the Kocks-Mecking-Estrin (KME) model. This model considers the dislocation density produced by deformation in twinned grains and non-twinned grains. The model was useful to explain the stress-strain interaction at microstructural scale but without taking into account the thermal effect. Chin et al. **[15]** and Hong et al. **[16]** used a finite element (FE) model to predict residual stresses in axial and tangential directions during the cup forming test in three TWIP steels with different Al content. Nonetheless, this model did not offer enough details about the material plastic behavior.

Due to the importance of residual stresses, as well as their magnitude and distribution, comprehensive methods are necessary to measure strain and residual stress in the welding of TWIP steels. A relationship between residual stress and changes in mechanical properties and microstructure is necessary to provide valuable information about weldability under specific operating parameters, particularly in TWIP steels.

Experimentally, the residual stress measurements through destructive (sectioning and contour method), semi-destructive (hole-drilling, ring core and deep hole) and non-destructive (Barkhausen noise, interferometry, X-ray diffraction, neutron diffraction and ultrasonic) techniques are limited **[17]**. Destructive techniques based on stress relief methods discard weld samples for subsequent test **[17-18]**. Besides, these techniques present a low resolution in deformation measurements **[17]**.

On the other hand, semi-destructive techniques only allow measuring residual stress on the surface. These techniques also require long test periods **[19]**. Regarding non-destructive techniques, neutron diffraction is a powerful method that allows obtaining larger penetration depth in the residual stress measurements. Its major drawback is the equipment cost **[17]**. On the contrary, methods based on X-ray diffraction have been widely used in several investigations **[20-22]** due to their capability to measure residual stresses at micro and macro scales **[17-18]** in weld joints.

Some studies on residual stresses have been developed by applying numerical solutions in order to analyze their effects on mechanical properties and microstructural defects in weldments **[23-25]**. Specifically, the Finite Element Method (FEM) has had a high acceptance to perform estimations of welding residual stress **[26]**. Nevertheless, numerical solutions have still limitations as computing cost, due to the complex non-linear analysis generated by the thermo-mechanical coupling and the lack of knowledge about the material properties at high temperatures **[27]**.

Thermo-mechanical numerical models used for estimation of residual stresses and distortion have been established by mathematical formulations for structural incompatibility representation, i.e., the strain gradient composed by elastic and non-elastic elements. For example, Deng et al. **[28]** used hardening models (isotropic, kinematic and mixed isotropic-kinematic) to estimate residual stresses in an AISI 304 steel weld butt joint performed in seventeen passes by the Gas Tungsten Arc Welding (GTAW) process. The mixed isotropic-kinematic hardening model, which considered the annealing temperature between weld passes, provided higher accuracy in its predictions. Brickstad et al. **[29]** applied a coupled FE thermo-mechanical model with a kinematic hardening rule to simulate residual stresses in a circumferential butt weld carried out in four weld passes. Akbari et al. **[21]** used another hardening models (isotropic, bilinear kinematic and elastic-perfectly plastic) to simulate the residual stress distribution in AISI 304 stainless steel welds with U-groove and V-groove joint preparations. In this case, the bilinear kinematic model provided the more accurate results.

The present research work is aimed to study the welding thermo-mechanical field of TWIP-Ti steel joints performed in 6.3 mm plate thickness. Regardless the welding process, low heat input has been proven by several authors to be the main factor to obtain a quality weld in TWIP steel **[2, 11-12]**. Accordingly, in the present work the welding process was carried out in two passes, which allowed using a low heat input. A numerical FE model was applied to estimate the residual stress and deformation magnitude/distribution in the weld joints. The FE simulation considered the application of two hardening models: isotropic and kinematic both bilinear and multilinear **[30]**. Then, it was determined the hardening rule to simulate residual stress development in the TWIP-Ti steel during the welding thermal cycle. The decoupled FE thermo-mechanical model assumed mechanical and thermophysical properties dependence on temperature to increase the accuracy **[31]**. The yield strength (YS) and ultimate tensile strength (UTS) were obtained at different strain rates and temperatures employing the JMatPro® 9.1 software. Furthermore, the temperature dependent tangent modulus (E_T) was calculated through the elastic modulus (E) and the ratio E_T/E as stated previously Mousavi et al. **[21]**. Residual stresses were measured experimentally through X-ray diffraction using the $\sin^2 \psi$ method **[32]**. These results were validated by the FE thermo-mechanical model. Additionally, microhardness measurements were taken from weldments applying the ASTM E 384 standard **[33]**. The residual stress critical zone (SCZ) was defined taking into account microhardness and residual stress distributions. The estimated stress magnitude in the SCZ was compared with the TWIP-Ti steel YS to determine the weld structural integrity.

2. Experimental procedure

Firstly, after casting the selected TWIP-Ti steel (Fe-22Mn-1.8Al-1.2Si-0.57C-0.0216Ti wt.%) was hot-rolled. Two thickness reduction passes of 60% and 50% were applied. The rolled plates were then solubilized (T= 1100 °C during 1200 s) followed by water quench. After that, weld samples were machined in blocks of following dimensions: $40 \times 20 \times 6.3$ mm (length, width and thickness). Weld joints were performed in two passes using the

GTAW process without supplying filler material. A double V-groove joint preparation was used (**Fig. 1**). **Table 1** shows the welding parameters used in each experiment.

Table 1. Autogenous GTAW process parameters used in the TWIP-Ti weldments.

Parameter:	Weldment 1	Weldment 2
Current intensity (A)	85	95
Voltage (V)	8.4	9.2
Welding speed (~~mm/s~~)	1.16	
Electrode type	EWTh-2	
Electrode diameter (mm)	1.6	
Arc length (mm)	1.5	

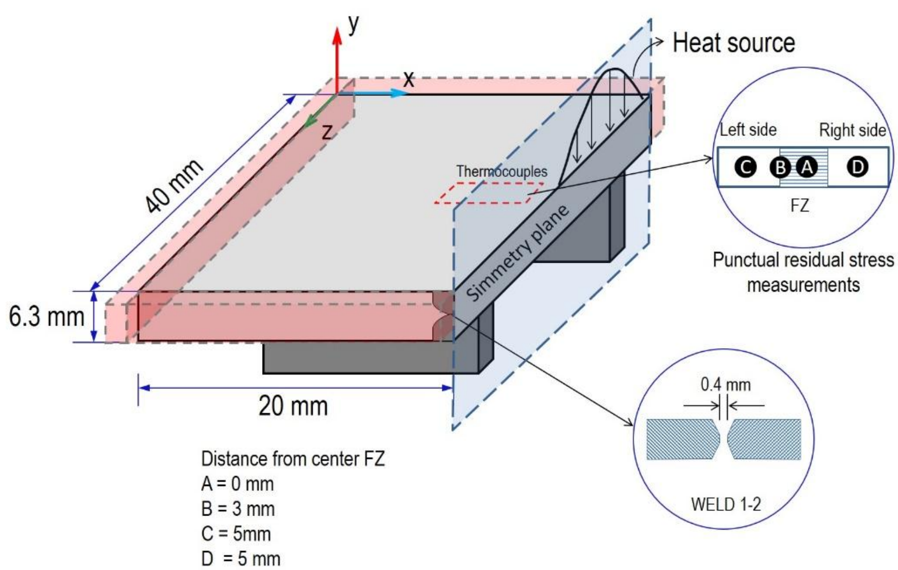

Figure 1. Set up for the GTAW process applied in the TWIP-Ti steel weld samples of 6.3 mm plate thickness.

Tack welds were applied in the four corners of the assembly (mechanical constraint) in order to avoid excessive distortion in weldments. The heat source traveled in opposite direction in every weld pass. The second weld pass was applied once the weldment reached the thermal equilibrium after the first weld pass.

During the welding process, the thermal cycle was recorded by means of a linear arrangement of K-type thermocouples and a TC-08 data acquisition (DAQ) modulus. Thermocouples were embedded to weld samples in the rear face to avoid altering the residual stress distribution. After every weld pass, the transverse deformation was measured through a dial indicator, once the weldment reached room temperature (**Fig. 2**).

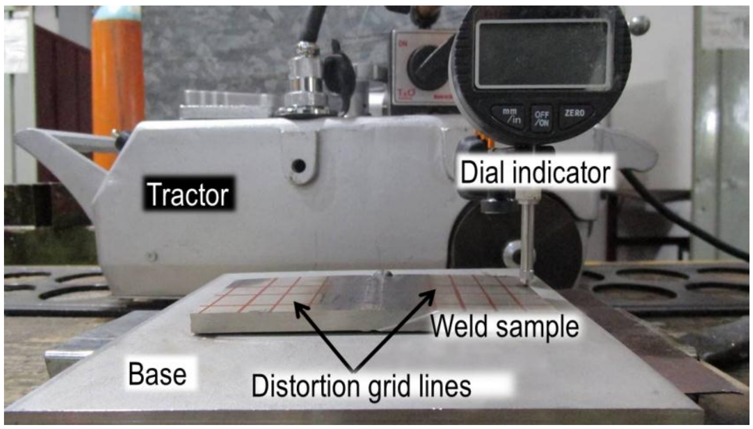

Figure 2. Set up for the post-welding transverse deformation measurement.

The post-welding residual stresses were experimentally measured through X-ray diffraction (using the $\sin^2 \psi$ method) in three points (A-C), as indicated in **Fig. 1**. These points were coincident with critical weld regions: center of FZ, FZ-HAZ interface and HAZ in both sides of the joint. The $\sin^2 \psi$ method calculates the residual stress as a function of the change in the lattice distance (D_0) between adjacent crystal planes **[32, 34]**. This distance is calculated by means of the Bragg's law:

$$2D_0 \sin\theta_0 = n\lambda \quad (1)$$

where n and λ are the diffraction order and the wavelength, respectively. The residual stress magnitude (σ) was calculated by means of the ψ angle (orientation angle between normal lines of crystal surface and sample), diffraction angle between X-ray and crystal surface (θ_0), diffraction angle at the orientation (θ_ψ), Poisson ration (v) and the diffraction angle (θ) according to the following equation **[34]**:

$$\sigma = \left[-\frac{1}{2}\, ctg\ \theta_0 \left(\frac{E}{v+1}\right)\right] \frac{\partial^2 \theta_\psi}{\partial sin^2 \psi} \quad (2)$$

X-ray diffraction patterns were recorded from $87.5° \leq 2\theta \leq$ ~~91.99~~. The high-intensity diffraction peak (311) was used to measure residual stress **[35]**. A step size of 0.015° 2θ and a counting time of 2 s per step were used (effective total time of 974 s).

Finally, transverse cuts of welded samples were carried out in order to perform the microstructural characterization by light optical microscopy (LOM) of critical weld regions. Also, microhardness measurements were taken from the cross section of weld samples applying a load of 10 g during 15 s and a step of 1500 μm.

3. FE Thermo-mechanical model

3.1. Thermal model

The temperature distribution was estimated by means of FE numerical solution of the heat equation (**Eq. 3**) using ANSYS Mechanical® software:

$$\rho C_P \frac{\partial T}{\partial t} = \nabla \cdot (\mathrm{k} \nabla T) + q_{f,r} \tag{3}$$

where ρ, C_p and k are the thermophysical properties; density, specific heat and thermal conductivity, respectively. While, $q_{f,r}$ represents the welding volumetric heat source. The assumptions of the mathematical model are listed below:

1. The volumetric heat source model proposed by Goldak et al. **[36]** was applied. The mathematical representation of double ellipsoidal volumetric heat source is given by:

$$q_{f,r}(x, y, \xi) = \frac{6\sqrt{3} f_{f,r} Q}{abc_{f,r}\pi\sqrt{\pi}} \exp\left(-3\left(\frac{x^2}{a^2} + \frac{y^2}{b^2} + \frac{\xi^2}{c_{f,r}^2}\right)\right) \tag{4}$$

This model considered the calculation of energy input rate (Q) by means of current intensity (I), voltage (V) and process efficiency (η), which was assumed of 70% for the autogenous GTAW process **[37]**. The parameters a (width), b (depth), c_f (front length) and c_r (rear length) correspond to the frontal and rear ellipsoids geometry. The weight functions f_f and f_r indicate the volumetric heat distribution. The global coordinates x, y, z were used as well as the non-inertial coordinate ξ. The travel of heat source in opposite directions in each weld pass was incorporated into the computational model through a programming code performed in Mechanical APDL®.

2. The TWIP-Ti steel thermophysical properties were considered temperature dependent. These were calculated by JMATPro® 9.1 software considering the chemical composition of the TWIP-Ti steel. Then, a curve fitting was applied and **Eqs. 5-7** were obtained for calculating the corresponding thermal conductivity (k), density (ρ) and specific heat (Cp).

$$k = 15.787 + 0.0135T \tag{5}$$

$$\rho = 7545.5 - 1.03T + 9.72 \times 10^{-4}T^2 - 5.6 \times 10^{-7}T^3 \tag{6}$$

$$Cp = 635 + 3229e^{\left(-2\left(\frac{T-1340.3}{66.23}\right)^2\right)} \tag{7}$$

3. Environmental heat losses by convection and radiation were considered as boundary conditions. The radiation heat loss was calculated through the following equation:

$$q''_{rad} = \varepsilon\sigma_B(T^4 - T_\infty^4) \tag{8}$$

where ε is the thermal emissivity (0.3) **[38]**, σ_B is the Stefan-Boltzmann constant ($\sigma_B = 5.67 \times 10^{-8}\ \cancel{W/m^2\ {}^\circ C}$) and T_∞ is the environment temperature. The convection heat loss was calculated using Newton's law of cooling ($q''_{conv} = hT - hT_\infty$). The heat transfer coefficient (h) was film temperature-dependent as stated by Garcia-Garcia et al. **[39]**.

4. The temperature before the first weld pass was the environment temperature (T_∞). Later, the second weld pass was carried out until the weldment reached the thermal equilibrium with the environment.

3.2 Mechanical model

Numerical results of the welding thermal field were linked to the mechanical field simulation to carry out estimations of residual stresses and deformation, i.e., the thermo-mechanical problem was solved decoupled. The non-linear calculation of welding residual stresses and deformation considered the incremental numerical solution **[30]** of the strain

(ε)-displacement ($\boldsymbol{u}$) relationship (**Eq. 9**), stress (σ) - strain (ε) (**Eq. 10**) and the mechanical equilibrium (**Eq. 11**).

$$\varepsilon = \boldsymbol{u}/L \tag{9}$$

$$\Delta\sigma = \frac{EH'}{E+H'}\Delta\varepsilon - \left\{\frac{EH'}{E+H'}\left(\alpha - \frac{1}{E^2}\frac{dE}{dT}\sigma\right) - \frac{E}{E+H'}\frac{d\sigma_Y}{dT}\right\}\Delta T - \frac{EH'}{E+H'}\dot{\varepsilon^c}\Delta t \tag{10}$$

$$\sigma_{ij} + \rho b_i = 0 \tag{11}$$

where H' and α are the strain hardening and thermal expansion coefficients, respectively. Meanwhile, σ_Y corresponds to TWIP-Ti steel's YS. The body force is represented by the product ρb_i in **Eq. 11**. On the other hand, the total strain ε^{total} is calculated as the sum of strains: i) thermal (ε^T), ii) elastic (ε^e), iii) plastic (ε^p) and iv) creep (ε^c) **[30]**.

$$\varepsilon^{total} = \varepsilon^T + \varepsilon^e + \varepsilon^P + \varepsilon^c \tag{12}$$

The vector u includes the nodal displacements in spatial coordinates (x, y, z) and L is a length scale. The assumptions applied to the mechanical model were:

- In the stress-strain analysis of welding, the elastic behavior was simulated by means of the Hooke law and the plastic behavior was solved through a rate independent plasticity model.
- The mechanical properties were temperature dependent (**Fig. 3**) to increase the accuracy of residual stress and deformation calculations **[31]**.
- The creep strain was neglected in the mechanical field simulation because to the heating time is very short **[40]**.
- Isotropic and kinematic hardening models were used to calculate the inelastic incompatibility produced during the welding thermal cycle.
- The Von Misses yield criterion **[41]** was applied in the mechanical model:

$$f\left(\sigma, \sigma_y\right) = \sigma_e - \sigma_y \quad \text{with} \quad \sigma_e = \sqrt{\frac{3}{2}\left(\sigma{:}\,\sigma - \frac{1}{3}\sigma^2\right)} \tag{13}$$

where σ_y is the yield strength and σ_e is the effective Von Misses stress **[41]**.

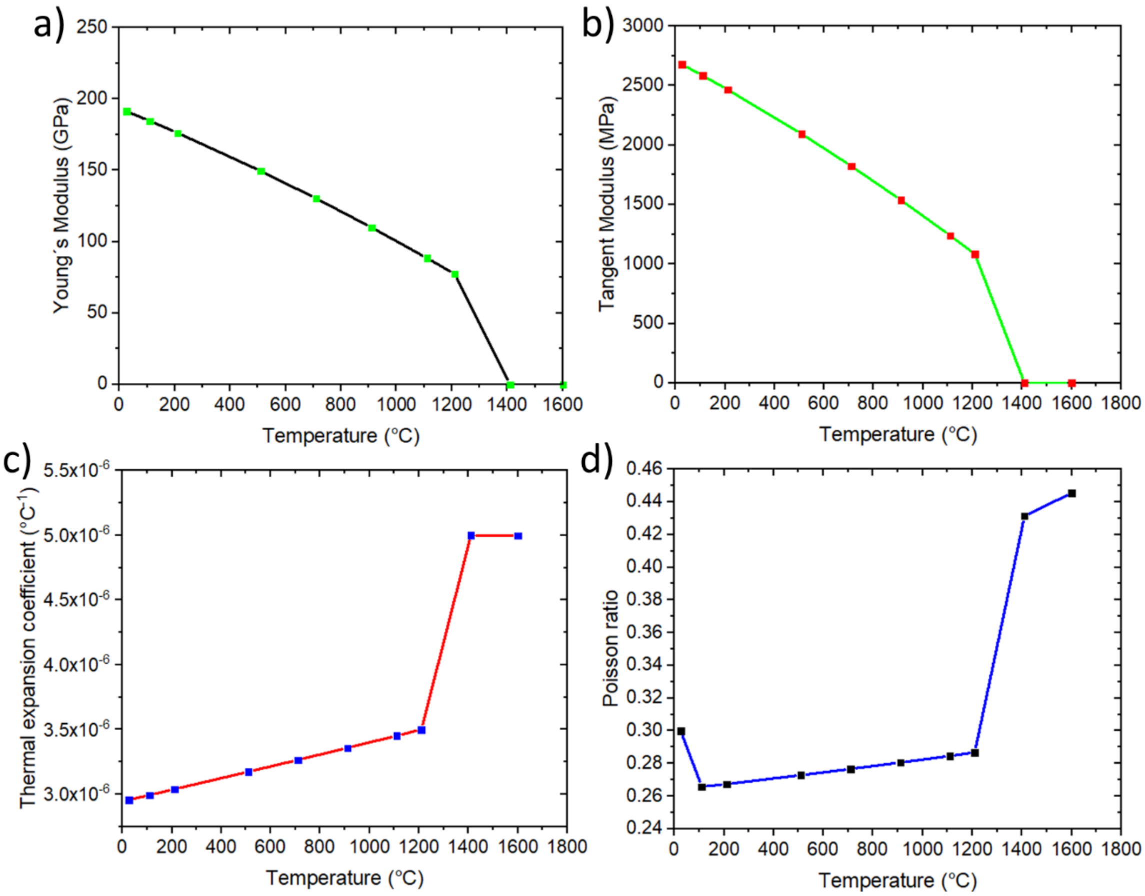

Figure 3. TWIP-Ti steel mechanical properties temperature dependent calculated by means of the JMatPro® 9.1: a) Young's modulus, b) Tangent modulus, c) Thermal expansion coefficient, d) Poisson ratio.

Applying the above assumptions to the mathematical model, the stress-strain equation (**Eq. 10**) and the total strain equation (**Eq. 12**) were modified as follows:

$$\Delta\sigma = \frac{EH'}{E+H'}\Delta\varepsilon - \left\{\frac{EH'}{E+H'}\left(\alpha - \frac{1}{E^2}\frac{dE}{dT}\sigma\right) - \frac{E}{E+H'}\frac{d\sigma_Y}{dT}\right\}\Delta T \qquad (14)$$

$$\varepsilon = \varepsilon^T + \varepsilon^e + \varepsilon^P \qquad (15)$$

The stresses must satisfy the equilibrium equation (**Eq. 11**) while the total strain (ε^{total}) must fulfill the compatibility condition (**Eq. 16**). When this condition do not equals zero, the incompatibility R exists, thus residual stress exists too (**Eq. 17**).

$$\left[\frac{\partial^2 \varepsilon_x'}{\partial y^2} + \frac{\partial^2 \varepsilon_y'}{\partial x^2} - \frac{\partial^2 \gamma_{xy}'}{\partial x \cdot \partial y}\right] + \left[\frac{\partial^2 \varepsilon_x''}{\partial y^2} + \frac{\partial^2 \varepsilon_y''}{\partial x^2} - \frac{\partial^2 \gamma_{xy}''}{\partial x \cdot \partial y}\right] = 0 \tag{16}$$

$$R = -\left[\frac{\partial^2 \varepsilon_x''}{\partial y^2} + \frac{\partial^2 \varepsilon_y''}{\partial x^2} - \frac{\partial^2 \gamma_{xy}''}{\partial x \cdot \partial y}\right] \tag{17}$$

Eq. 18 is the plastic flow rule associated with the model yield surface: isotropic and kinematic. This rule represents the plastic strain evolution in relation with the plastic potential (Q) and the non-elastic strain increment ($d\lambda$).

$$d\varepsilon^p = d\lambda \frac{\partial Q}{\partial \sigma} \tag{18}$$

The interaction between thermal stresses ($\sigma_{i,j}$) and the thermal strain (ε^t) was calculated through the next equation:

$$\varepsilon_{ij} = \frac{1+\nu}{E}\sigma_{ij} - \frac{\nu}{E}\sigma_{kk}\delta_{ij} + \lambda s_{ij} + \left[\alpha + \frac{\partial \alpha}{\partial T}(T - T_0)\right] dT \tag{19}$$

Fig. 4 shows the engineering stress-strain curves estimated by JMatPro® 9.1 for TWIP-Ti steel at different temperatures and strain rates: 0.001 s^{-1}, 0.01 s^{-1}, 0.1 s^{-1}, 1 s^{-1}, 10 s^{-1} and 100 s^{-1}. Stress-strain curves were used for the material specification into the mechanical model, which was solved numerically in ANSYS Mechanical®. In addition, engineering stress-strain curves predicted by JMatPro® 9.0 software presented a reasonable agreement with previous experimental results reported by Jung et al. **[42]**. They performed uniaxial tensile tests on Fe-17Mn-0.62C-0.01Si-0.08Ti TWIP steel using a strain rate of 0.001s^{-1} and a temperature range of ~~100°C~~ up to ~~800°C~~. **Fig. 5** shows the comparison between stress-strain curves obtained experimentally in **[42]** and the estimations performed through JMatPro® 9.0 software. The variation of normal stress magnitudes decreases at higher temperatures (**Fig. 5**), which is desirable to enhance the FE simulation accuracy of residual stress distribution in welding zones with higher temperature gradient.

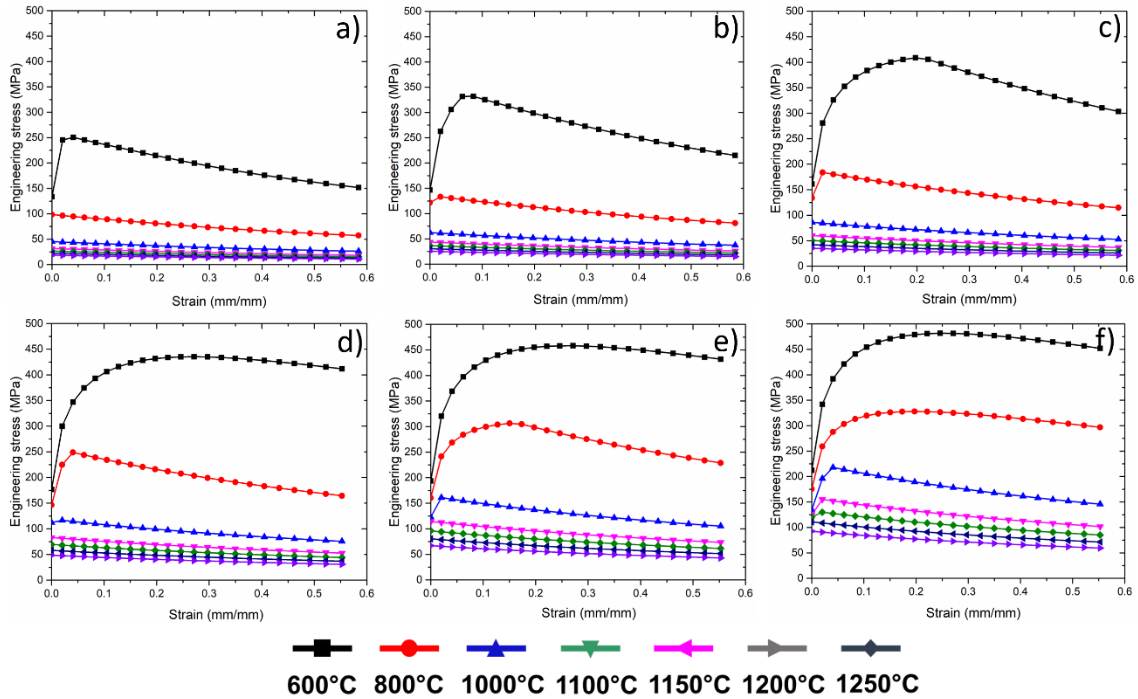

Figure 4. Engineering stress-strain curves of TWIP-Ti steel at different temperatures and strain rates of: a) 0.001 s^{-1}, b) 0.01 s^{-1}, c) 0.1 s^{-1}, d) 1 s^{-1}, e) 10 s^{-1} and f) 100 s^{-1}.

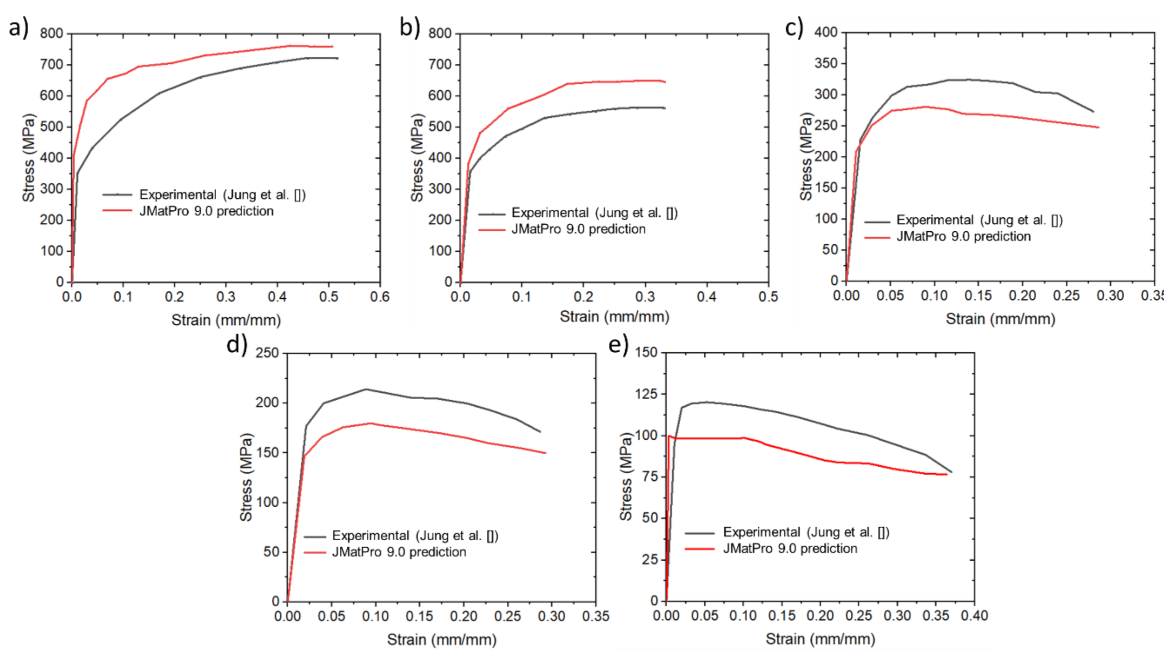

Figure 5. Validation of engineering stress-strain curves estimated through JMatPro® 9.1 software with tensile tests experimental data carried out at a strain rate of ~~0.001s^{-1}~~ and different temperatures: a) ~~300°C~~ b) ~~400°C~~ c) ~~600°C~~ d) ~~700°C~~ e) ~~800°C~~.

At higher temperatures (>~~800°C~~), the mechanical strength of TWIP-Ti steel exhibited a steep decrease, as shown in **Fig. 4**. This strength reduction agrees with the results reported by Hamada et al. **[43]**. Besides, at higher temperatures (>~~900°C~~), the elongation increases due to dynamic recrystallization **[43]**. The increasing temperature (>~~300°C~~) generates a stacking fault energy (SFE) increment **[44]**, which inhibits mechanical twinning and only dislocation glide occurs **[45]**.

For bilinear hardening models (isotropic and kinematic) the parameters C1 and C2 (strain hardening coefficient) were defined, as shown in **Fig. 6**. These parameters, C1 and C2, corresponding to the YS and strain-hardening coefficient, respectively. The stress-strain curves of TWIP-Ti steel provide the YS at different temperatures and strain rates (**Fig. 4**). Meanwhile, the strain-hardening coefficient was calculated as indicates in **Fig. 6a**. For multilinear hardening models (isotropic and kinematic), the variation of plastic strain-stress relationship was defined in order to determine the parameters Pi (normal stress) and Pj (plastic strain) (see **Fig. 6**). The multilinear behavior is characterized by a series of elasto-perfectly plastic lines at different points (Pi, Pj) **[46]**.

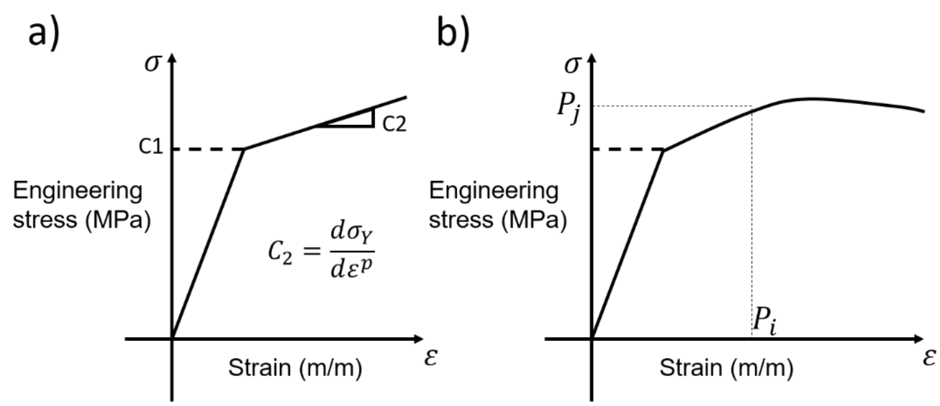

Figure 6. a) Bilinear stress-strain relationship, b) Multilinear stress-strain relationship.

Temperatures were defined as thermal loads through the programming code done in Mechanical APDL®. Meanwhile, essential boundary conditions were the tack welds applied in sample corners (**Fig. 7a**), which restrained the displacements in the calculation domain (**Fig. 7b**).

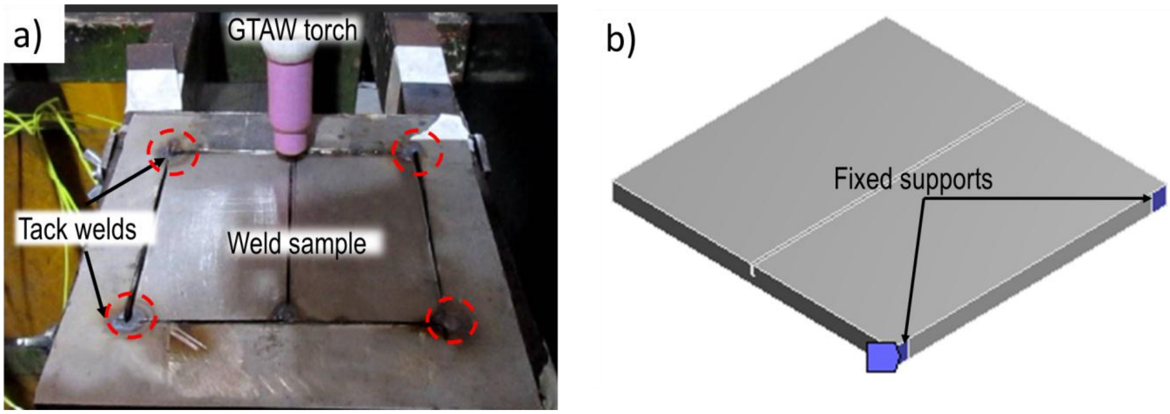

Figure 7. a) Tack welds applied in corners of TWIP-Ti steel plates, b) Essential boundary conditions applied into the calculation domain.

3.3 Mesh and computational solution

In the FE thermo-mechanical model two meshes with similar topologies were used to ease the results transfer from the thermal field to the mechanical. The mesh used for thermal model was formed by 40680 hexahedral elements type SOLID90 and 178525 nodes. While, the mechanical model mesh had the same number of nodes and elements but, type SOLID186 recommended for simulation of elastoplastic materials **[46]**. Mesh element sizes of 0.3 mm, 0.5 mm and 0.8 mm (with a bias factor of 6) were applied to the discretization of FZ, HAZ and base material (BM), respectively (**Fig. 8a**).

The mesh metric was measured considering the parameters: skewness and orthogonal quality. **Figs. 8b** and **8c** show the mesh element distribution graphs as a function of quality parameters. The orthogonal quality was close to 1 and the skewness tended to zero indicating quality meshes **[46]**.

A mesh-independent solution was achieved for the FE welding thermal model. **Fig. 8d** shows the comparison between temperature estimations obtained by three FE meshes (with different number of elements) and the experimental thermal history measured in the point A near to the FZ.

The numerical solution of the welding thermal model was obtained in 3090 iterations using a time step of 0.5 s and a tolerance of 0.1% for the heat convergence criterion. On the other hand, the solution of the mechanical model was achieved after 5600 iterations and a tolerance of 1% for the force convergence criterion. The computational model was solved in a workstation with Intel Core i7-6500U 3.1 GHz 16GB RAM processor.

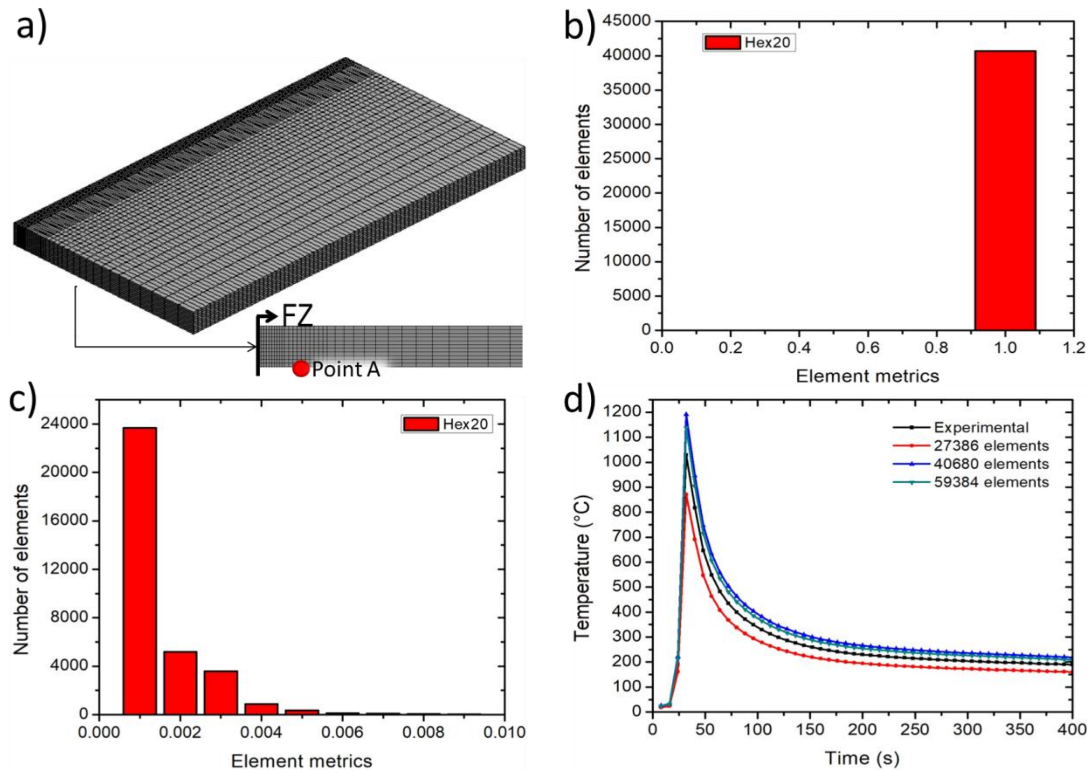

Figure 8. a) Mesh used in the welding thermal and mechanical models, b) Mesh elements orthogonal quality distribution, c) Mesh elements skewness distribution, d) Mesh-independent solution study in the thermal model.

4. Results and discussion

The FE thermo-mechanical model assessed the isotropic and kinematic hardening models to simulate the elastoplastic behavior of the TWIP-Ti steel during the welding thermal cycle. **Fig. 9** shows the longitudinal residual stress distribution estimated by the FE thermo-mechanical model at different cross-section points of the welded joint 1 considering a strain rate range of 0.001 – 100 s^{-1} (**Fig. 4**).

As can be seen in **Fig. 9**, all hardening models predicted almost the same magnitudes for tensile residual stresses in the FZ (0-5 mm) regardless of the strain rates. However, the residual stress estimations in the HAZ and BM (5-40 mm) exhibited variations with the strain rate in each hardening model (**Fig. 9**). These results were in good agreement with the engineering stress-strain curves estimated by JMATPro® 9.1 software (**Fig. 4**). At higher temperatures (>~~1000°C~~), the mechanical strength of TWIP-Ti steel is low and almost the same for all strain rates, as shown in **Fig. 4**. On the other hand, the more significant variations in the mechanical strength of TWIP-Ti steel are found at low temperatures (<~~1000°C~~).

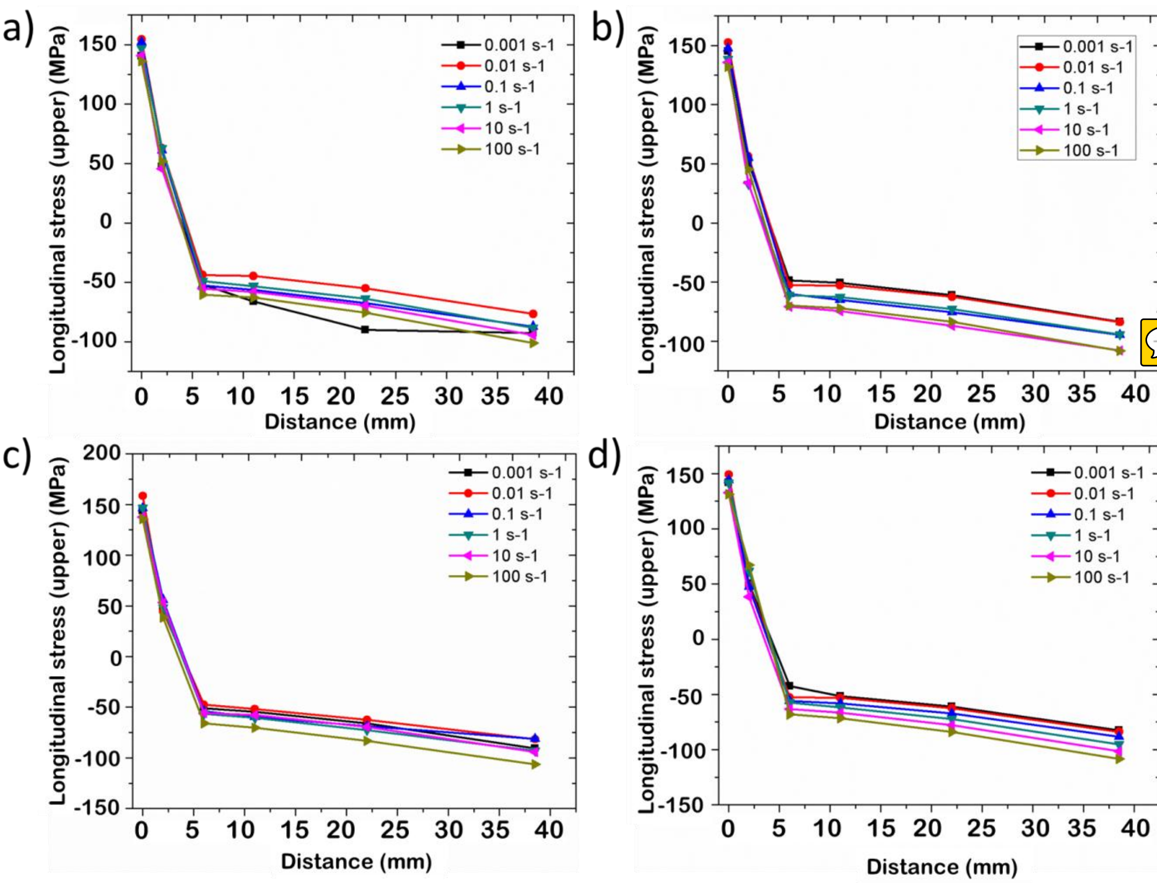

Figure 9. Longitudinal residual stress estimated at different strain rates by different hardening models: a) Bilinear isotropic, b) Multilinear isotropic, c) Bilinear kinematic, d) Multilinear kinematic.

As already mentioned, both strain hardening models (isotropic and kinematic) depend on mechanical strength constants (YS, E, E_T, strain-hardening coefficient, ultimate tensile strength, etc.,), which change with temperature. In the FZ, the higher temperatures (>~~1000°C~~) generated almost the same magnitudes of residual stresses due to the low mechanical strength of TWIP-Ti steel (**Fig. 9**). While in HAZ and BM, the lower temperatures (<~~1000°C~~) and the mechanical strength recovery (**Fig. 4**) generated different residual stresses depending on the strain rate (**Fig. 9**).

A similar trend was exhibited for the numerical results of both hardening models. Tensile residual stresses were concentrated in the FZ-HAZ, while compressive stresses were found in regions far away from the FZ **[7, 28]**. The literature points out that the isotropic model tends to overestimate stress magnitudes, while the kinematic model predicts inferior magnitudes **[47]**. As already noticed, the FE simulation of residual stresses considered stress-strain curves at different strain rates. The results showed that in general terms, and in most hardening models, the strain rate of 0.001 s^{-1} provided the higher tensile stresses and the lowest compressive stresses (**Fig. 9**). Conversely, the strain rate of 100 s^{-1} generated the lowest tensile stresses and the higher compressive stresses.

Table 2 shows maximum/minimum residual stresses estimated by the different hardening models at different points of weldment from FZ to BM. The strain rate at which the maximum/minimum residual stress was predicted is indicated in parenthesis (**Table 2**). A variation of 6% in the maximum tensile stress between the bilinear kinematic model (158 MPa) and the multilinear kinematic (149 MPa) was found. On the other hand, the maximum difference between the higher compressive stress was of 7% between the multilinear kinematic model (-108.5 MPa) and the bilinear isotropic (-101 MPa). The variation in the residual stress estimations performed by both hardening models are relatively small (**Table 2**) and can be neglected.

The multilinear kinematic model was selected to simulate the evolution of residual stresses and deformation during welding thermal cycle in TWIP-Ti steel plates. In spite of the small variations between multilinear isotropic and multilinear kinematic models (**Table 2**), it is accepted in the literature that the kinematic model is the most accurate for welding residual stress prediction **[47-48]**. Besides, the strain rate of 0.1 s^{-1} provided average estimations between maximum and minimum residual stresses for all hardening models (**Fig. 9**). Therefore, the strain rate of 0.1 s^{-1} was used to simulate the residual stresses in the TWIP-Ti steel weld joint.

Table 2. Tensile and compressive residual stresses estimated by the isotropic and kinematic hardening models at different strain rates.

Longitudinal residual stress (MPa)							
Bilinear isotropic		Multilinear isotropic		Bilinear kinematic		Multilinear kinematic	
Maximum	Minimum	Maximum	Minimum	Maximum	Minimum	Maximum	Minimum
(strain rate, s^{-1})		(strain rate, s^{-1})		(strain rate, s^{-1})		(strain rate, s^{-1})	
154.38 (0.01)	136 (100)	152.54 (0.01)	132.04 (100)	158.49 (0.01)	135.93 (100)	149.29 (0.01)	131.19 (100)
62.82 (0.01)	45.74 (10)	56.38 (0.01)	32.96 (1)	55.84 (0.1)	38.6 (100)	67.16 (100)	38.3 (10)
-43.73 (0.01)	-60.5 (100)	-48.61 (0.001)	-70.79 (10)	-47.49 (0.01)	-65.79 (100)	-42.29 (0.001)	-68.08 (100)
-44.72 (0.01)	-66.2 (0.001)	-50.55 (0.001)	-74.44 (10)	-51.88 (0.01)	-70.37 (100)	-51.52 (0.001)	-71.53 (100)
-54.87 (0.01)	-90 (0.001)	-61.07 (0.001)	-86.76 (10)	-62.51 (0.01)	-83.28 (100)	-61.21 (0.001)	-83.82 (100)
-76.62 (0.01)	-101 (100)	-83.59 (0.001)	-108 (100)	-81.32 (0.1)	-106.45 (100)	-82.48 (0.001)	-108.49 (100)

Residual stresses were experimentally measured by means of X-ray diffraction in critical weld regions (**Fig. 1**). These results were compared with numerical estimations carried out by the FE thermo-mechanical model, applying the multilinear kinematic hardening model at a strain rate of 0.1 s^{-1}. **Fig. 10** shows these comparisons in both sides of the weldment. It should be noted that only the residual stress measurement for the HAZ (point C in **Fig. 1**) is accurate (**Fig. 10)**. However, in the FZ and the FZ-HAZ interface (points A and B, respectively in **Fig. 1**), the residual stress measurements exhibited high deviation ($> 260\ MPa$) (**Fig. 10**). This high deviation was associated with the presence of a diffraction peak of δ-ferrite (121) near to the austenite peak at $2\theta = 89.7°$, as shown in **Fig. 11**. In fact, the (110), (002) and (121) diffraction peaks (δ-ferrite) were detected at different points in the FZ (**Fig. 12b**). According to the TWIP steel equilibrium phase diagram **[2, 49]**, the δ

-ferrite phase is a high-temperature phase and unstable at room temperature. Nonetheless, the high cooling rates produced in welding allowed solidifying a remnant fraction of δ-ferrite in FZ. On the contrary, all the XRD patterns recorded from HAZ and BM only presented diffraction peaks of austenite (**Fig. 12a**).

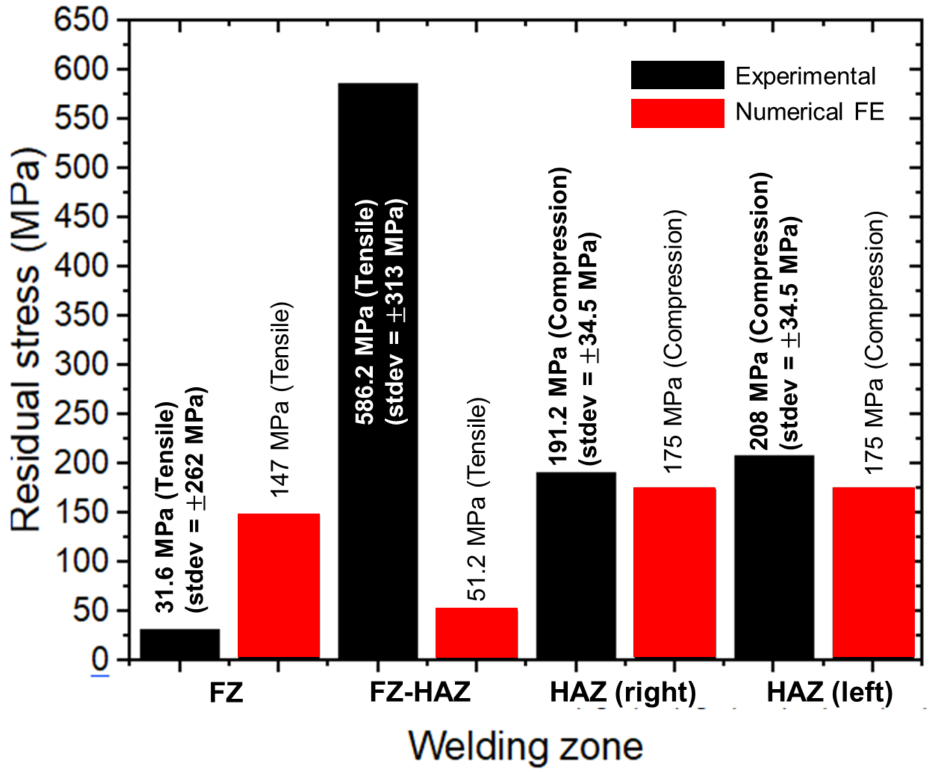

Figure 10. Residual stress estimated numerically vs X-ray diffraction measurements ($\sin^2 \psi$ method) for welded joint 1.

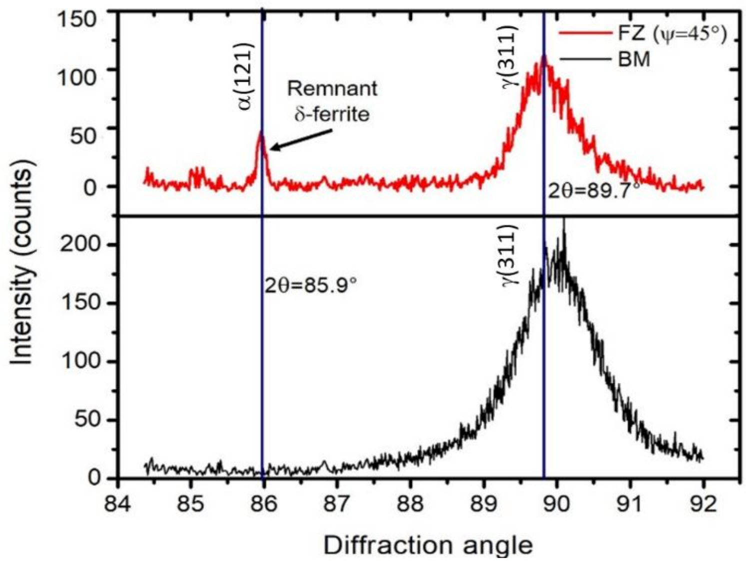

Figure 11. Diffraction peak ($2\theta = 89.7°$) analyzed for residual stress measurements in FZ.

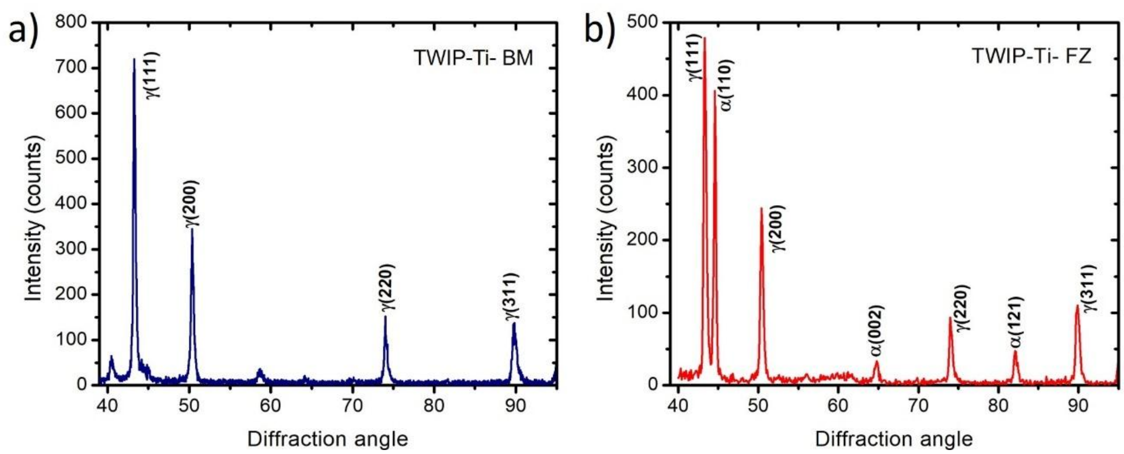

Figure 12. Diffraction profiles obtained from: a) BM, b) FZ.

The residual stress measured experimentally in the HAZ showed a good agreement with the FE estimations (**Fig. 10).** A deviation of 8.5% between experimental and numerical models was obtained. This level of deviation (8.5%) is almost negligible considering some previous research works with higher variations in residual stress measurements between experimental and numerical results. For instance, Abdulkareem et al. **[50]** reported an average variation of 32% in FE residual stress predictions as compared to the experimental measurements (hole-drilling method). Meanwhile, Heinze et al. **[51]** obtained variations in longitudinal and transverse residual stresses of more than double between experimental measurements (X-ray diffraction method) and FE estimations.

In this case, the deviation corresponded to the right side of the weldment. This variation can be associated with the uneven distribution of the inelastic deformation in welding, which produced different magnitudes of residual stress in comparable points at opposite sides of the weldment. Meanwhile, the FE thermo-mechanical model applied a symmetry condition to reduce computing time. In adjacent regions to the FZ, where temperatures are higher, the grain size in TWIP-Ti steel exhibits high heterogeneity **[52]**. This affects mechanical properties and thus the residual stress magnitude. However, the grain size heterogeneity is difficult to consider in the simulation of the welding mechanical field. In the FE model, the only variation in mechanical properties was generated by the welding thermal cycle.

Figures 13-14 show the numerical estimation of longitudinal residual stress distribution during thermal cycle in weldments 1 and 2. The results show clearly the change from tension to compression in weldments depending on the heat source displacement over the workpiece (**Figs. 13a-b** and **14a-b**). During the cooling stage, stresses start to stabilize and exhibit the typical distribution in welding (**Figs. 13d** and **14d**): tensile stresses in FZ and compressive stresses in distant regions **[8, 19, 21]**. Tensile stresses were predicted in the upper part of both weldments and compressive stresses in the lower part after the second weld pass (**Figs. 13d** and **14d**), these observations were consistent with results reported by Teng et al. **[53]**. In the weldment 1 (higher heat input) higher residual stresses were produced (**Figs. 13** and **14**) in agreement with literature **[9, 21]**.

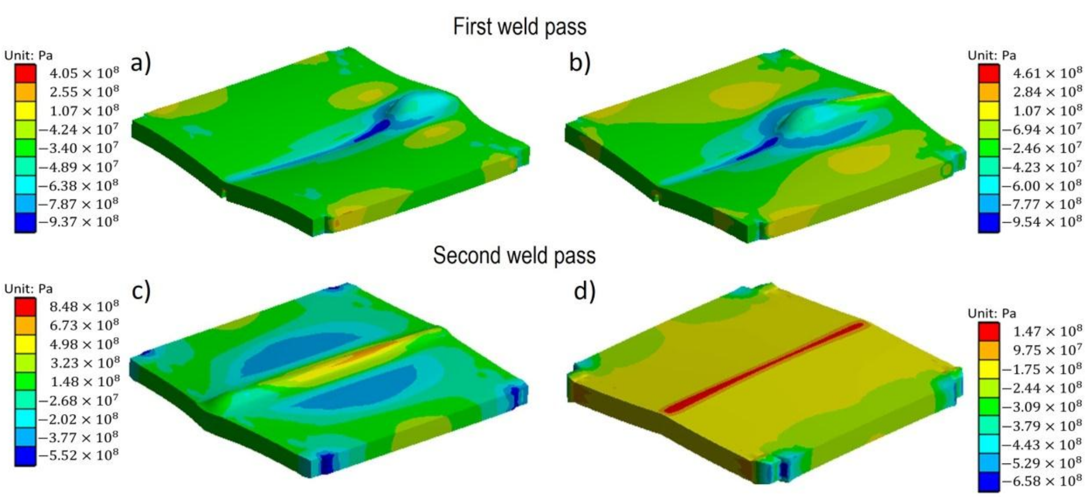

Figure 13. Longitudinal residual stress transient distribution estimated by the FE thermo-mechanical model (multilinear kinematic hardening model) in TWIP-Ti steel weldment 1 (461 ~~J/mm~~): a) 10 s, b) ~~25s~~, c) 70 s, d) 600 s.

The comparison of longitudinal residual stress estimated with experimental results reported by Mujica et al. **[12]** for a dissimilar weld TWIP-TRIP showed also a reasonable agreement. Mujica et al. **[12]** measured a maximum longitudinal tensile stress of 180 MPa near to the FZ for a heat input of 300 ~~J/mm~~. In this research work, maximum longitudinal tensile stresses of 245 MPa and 147 MPa were estimated for heat inputs of 565 ~~J/mm~~ and 461 ~~J/mm~~, respectively. These stresses were affected by welding parameters, plate thickness and mechanical constraint level.

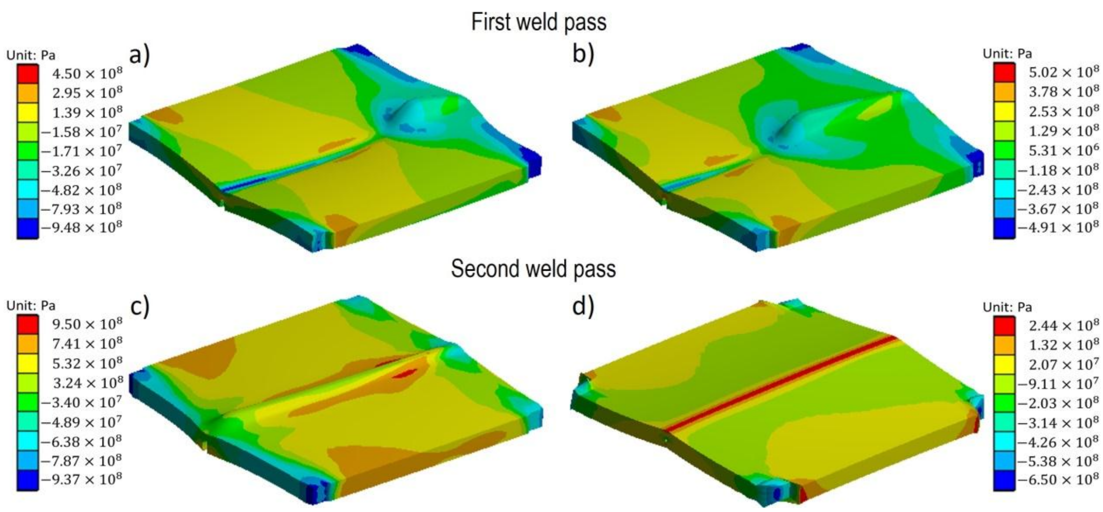

Figure 14. Longitudinal residual stress transient distribution estimated by the FE thermo-mechanical model (multilinear kinematic hardening model) in TWIP-Ti steel weldment 2 (565 ~~J/mm~~): a) 10 s, b) ~~25s~~, c) 70 s, d) 600 s.

Fig. 15 shows the numerical estimation of transverse residual stresses obtained after the first pass in TWIP-Ti steel weldments. Again, it was observed the direct relationship between temperature and residual stresses.

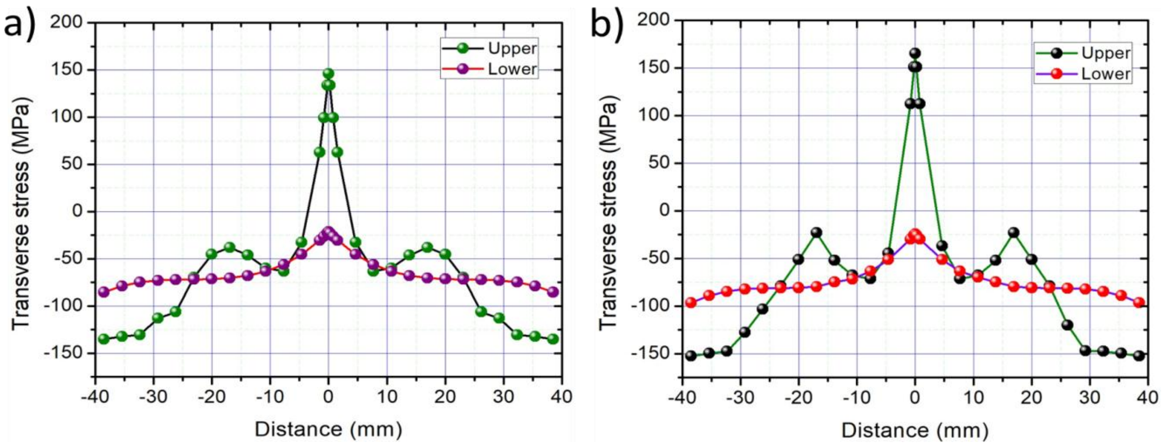

Figure 15. Post-welding transverse residual stress distribution (first pass) estimated in the upper and lower faces of TWIP-Ti steel weldments: a) 461 ~~J/mm~~, b) 565 ~~J/mm~~.

Tensile stresses were generated in the upper face of weldments where the thermal energy had a higher concentration. It should be noted that magnitudes of compressive stresses in the rear face were not equal to tensile ones (**Fig. 15**). This was due to the V-groove joint which reliefs the residual stress (**Figs. 13a-b** and **14a-b**).

The maximum tensile residual stresses in FZ were correlated with transverse microhardness values, which were measured in the mid-plane of the low heat input weldment. According to microhardness results for weldments 1 and 2 (**Fig. 16a** and **b**), the FZ and part of the HAZ were coincident with the maximum tensile stress region, as shown in **Fig. 16c**. This region was named residual stress critical zone (SCZ). The microhardness in the HAZ decreased as compared to the BM (**Fig. 16a** and **b**). In this region, it was produced the curvature change of tension stress zone. At the same time, it started to decrease the residual stress until reached the compressive zone (**Fig. 16c**). This region was coincident with the parent material. Previously, Lemos et al. **[54]** and Rae et al. **[55]** also reported similar trends in the distribution curves of residual stress-microhardness.

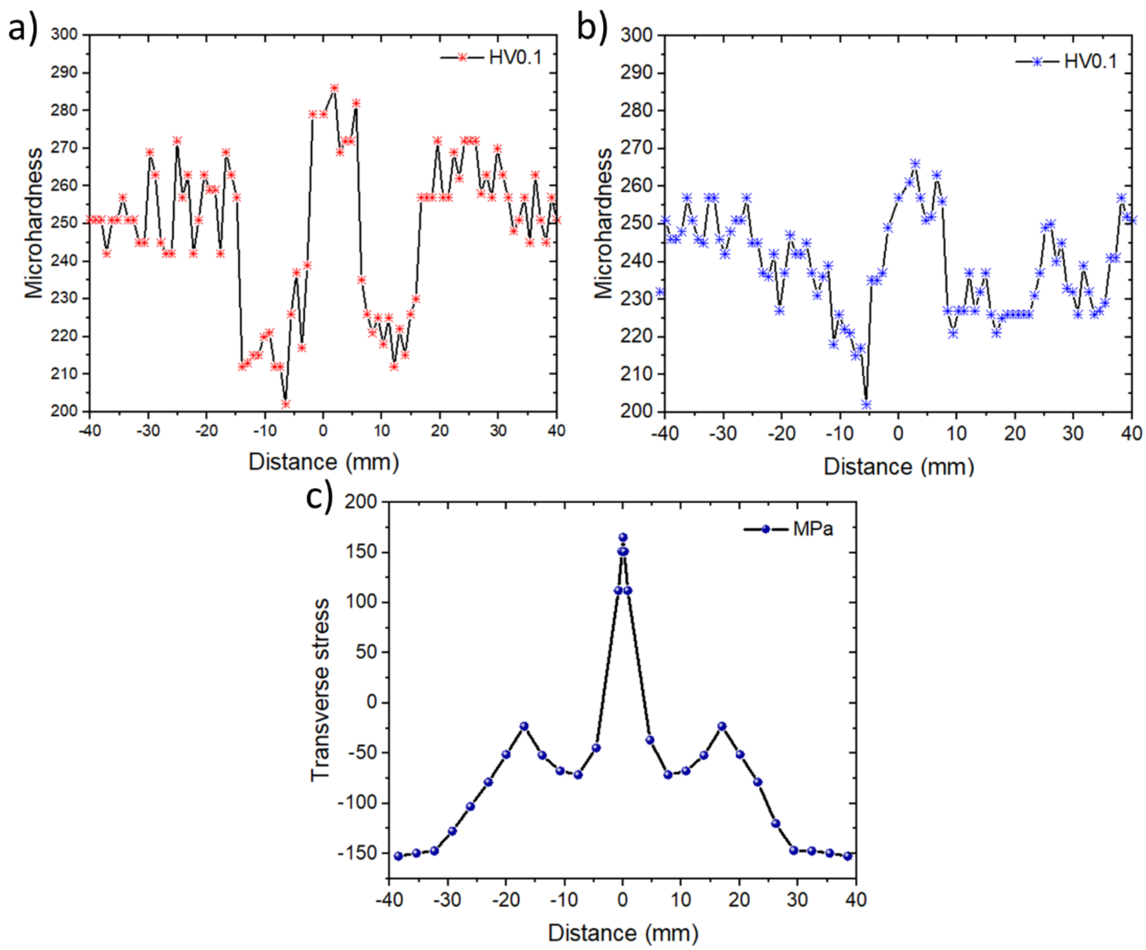

Figure 16. Microhardness profiles: a) weldment 1 (461 ~~J/mm~~), b) weldment 2 (565 ~~J/mm~~), c) Transverse residual stress distribution in the mid-plane of the TWIP-Ti weldment of low heat input (461 ~~J/mm~~).

In the present TWIP-Ti steel, the higher tensile residual stresses estimated in the SCZ were related to the thermal diffusivity distribution, which is temperature-dependent. **Fig. 17** shows estimations of temperature distribution, thermal conductivity (k) and thermal expansion coefficient (α) in TWIP-Ti steel weldments. It is important to bear in mind that TWIP-Ti steel presents a thermal-insulating behavior, that is, when the temperature decreases, the TWIP-Ti steel thermal diffusivity diminishes too. Hence, a low heat flux diffuses from the FZ to distant regions. Heat concentrates in FZ and adjacent region (**Fig. 17**).

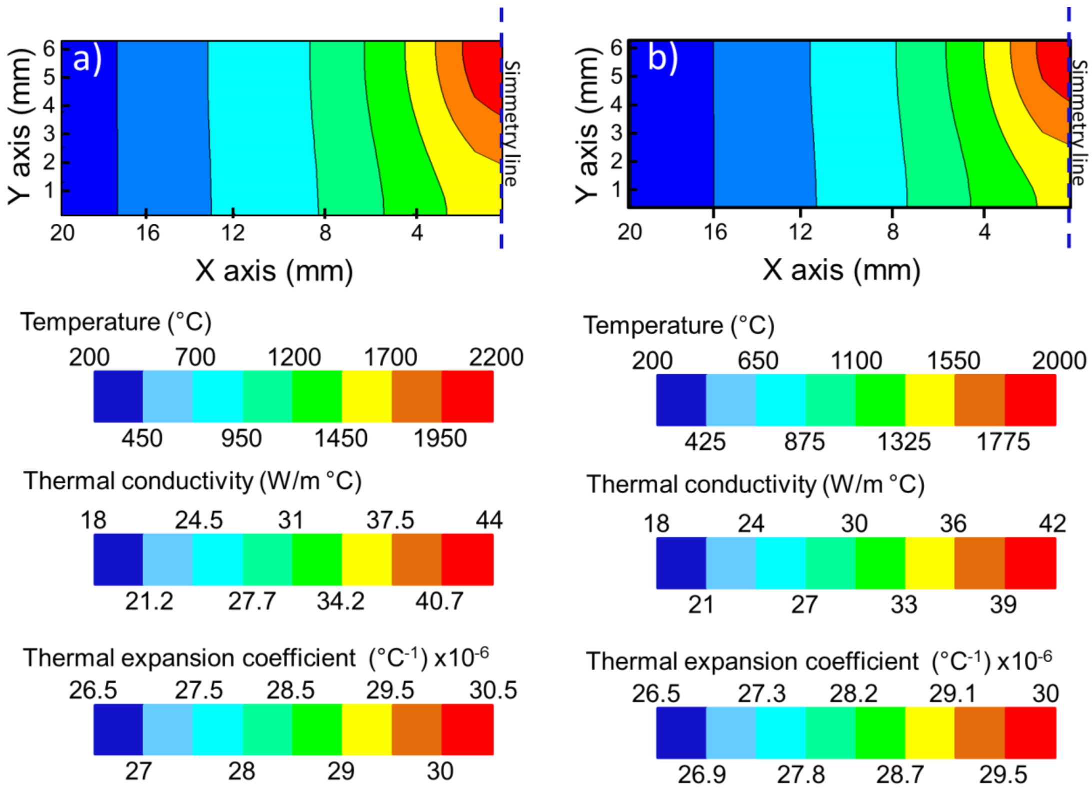

Figure 17. 2-D contours of temperature distribution, thermal conductivity and thermal expansion coefficient in TWIP-Ti steel weldments: a) 565 ~~J/mm~~, b) 461 ~~J/mm~~.

In high temperature regions, the high thermal expansion coefficient (**Fig. 17**) brought about high thermal stresses, which diminished in faraway regions of FZ. This decrement in both thermal diffusivity and expansion coefficient generated low compressive stresses as compared to the tensile ones (**Fig. 13-15**).

Ishigami et al. **[8]** pointed out the combination of high residual stresses and hardness was deleterious for the weldment structural integrity. Particularly in TWIP-Ti steel weldments, hot cracking is an undesirable effect generated by the C and Mn segregation in both FZ and HAZ **[2, 11]**. Micro-cracks produced during solidification stage can propagate toward the adjacent region as a result of high residual stresses. Also, surface cracks in the weld bead can produce due to the combined effect of hardening and residual stress.

However, the transverse peak tensile stress in the SCZ estimated in weldment 1 was of 145 MPa (**Fig. 16c**). In comparison with the TWIP-Ti steel YS of 398 MPa **[52]**, the peak tensile stress in the SCZ does not affect the weldment structural integrity. The same can be established from the maximum transverse tensile residual stress (149 MPa) in the SCZ of weldment 2 compared with the TWIP-Ti steel YS.

The average hardness in the SCZ was diminished by the HAZ (**Fig. 16a** and **b**). In weldment 2 both transverse and longitudinal stresses are higher than in weldment 1 (**Figs. 14d** and **15b**). The hardness of the SCZ in weldment 2 also diminished by the HAZ (**Fig. 16b**). Therefore, there were not conditions to promote hot-cracking in TWIP-Ti weldments. In TWIP-Ti steel weldments, the Al-content helped to reduce the activity and diffusivity of C and Mn. The above inhibited the formation of the eutectic compounds as $(C, Mn)_3Fe$ in the FZ-HAZ interface. These compounds are responsible for the formation of liquation cracks in the HAZ of TWIP steel welds **[2]**. The aforementioned was corroborated by means of LOM analysis in the FZ and FZ-HAZ interface of weldment 1, as shown in **Figs. 18a** and **b**. Hot-cracking was not found in the weld beads nor liquation cracks on both sides of the FZ-HAZ interface.

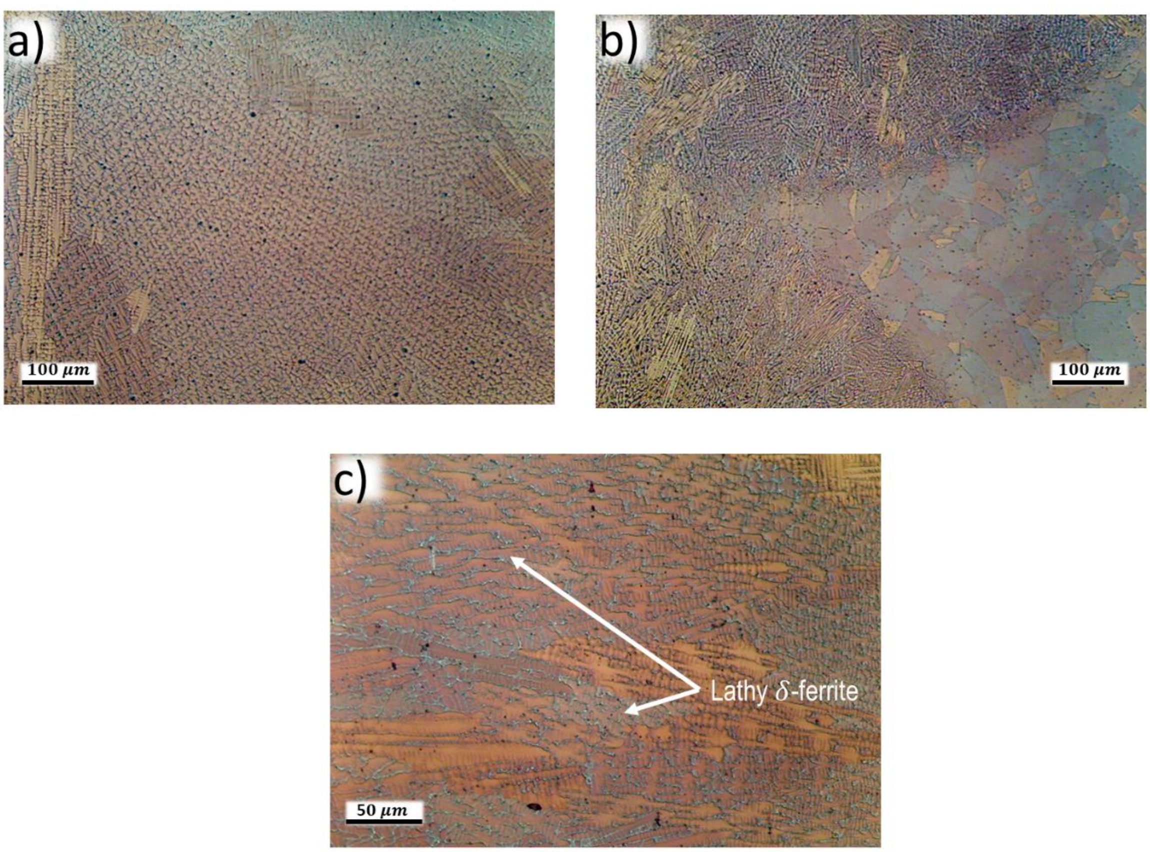

Figure 18. Microstructural observations of the TWIP-Ti weldment 1: a) FZ-center, b) FZ-HAZ interface, c) Remnant δ-ferrite found in FZ boundary (weldment 1).

In all TWIP-Ti steel weldments, predominantly lathy ferrite morphology was observed in the as-welded region. The δ-ferrite was precipitated in the inter-dendritic region, as shown in **Fig. 18c**. This could be associated with the epitaxial growth of the grain in the fusion zone, which usually originates from the BM grains and grows in the direction of maximum heat flow (from FZ boundary to HAZ).

The heat concentration detected in FZ and adjacent zones (**Fig. 17**), as well as the increase in thermal expansion coefficient, were in good agreement with plastic strain estimations. **Fig. 19** shows the plastic strain evolution with thermal cycle in weldment 1. During the heating stage, thermal expansion generated high plastic strain in the FZ and adjacent regions (**Figs. 19a** and **c**). Once the thermal equilibrium was reached, the plastic strain was concentrated in constraint points due to the weldment expansion. The expansion in FZ and adjacent regions brought about the groove loss in the weldment rear face after the first weld pass (**Fig. 1**).

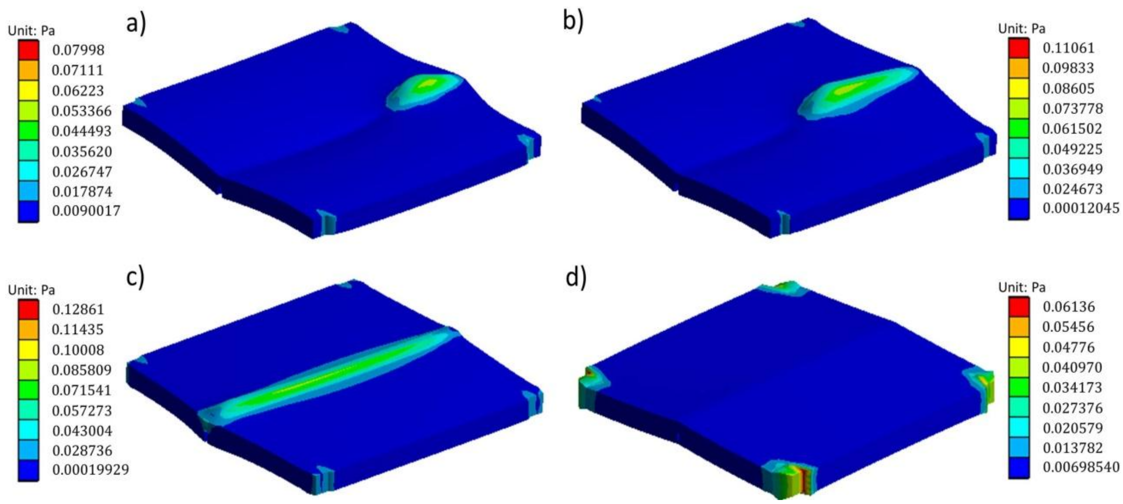

Figure 19. Welding plastic strain transient distribution estimated by the FE thermo-mechanical model (with multilinear kinematic hardening model) in TWIP-Ti steel weldment 1 (461 ~~J/mm~~) at: a) 10 s, b) 25 s, c) 70 s, d) 600 s.

An under-filling in the weld seam owing to the autogenous GTAW process was detected by means of deformation measurements (**Fig. 20**). After the second weld pass, deformation measurements were taken (**Figs. 20b** and **c**). The small variations in the measurements of lines L3 and L1 during the first and second weld pass were associated with the welding sequence and the heat concentration.

The application of mechanical constraints into the weldments modifies deformation and produces a residual stress increment **[56]**. The V-groove loss indicated that the constraint applied was relatively low, since the constraint limited both longitudinal and transverse displacements but, it did not avoid angular rotations (**Fig. 20**). After the welding process application, the plastic strain was localized in constraint points (**Fig. 19**) inside the compressive stress region. The plastic strain did not generate any localized effect into the residual stress distribution in the SCZ as reported by Khandkar et al. **[57]** in austenitic stainless-steel weld joints.

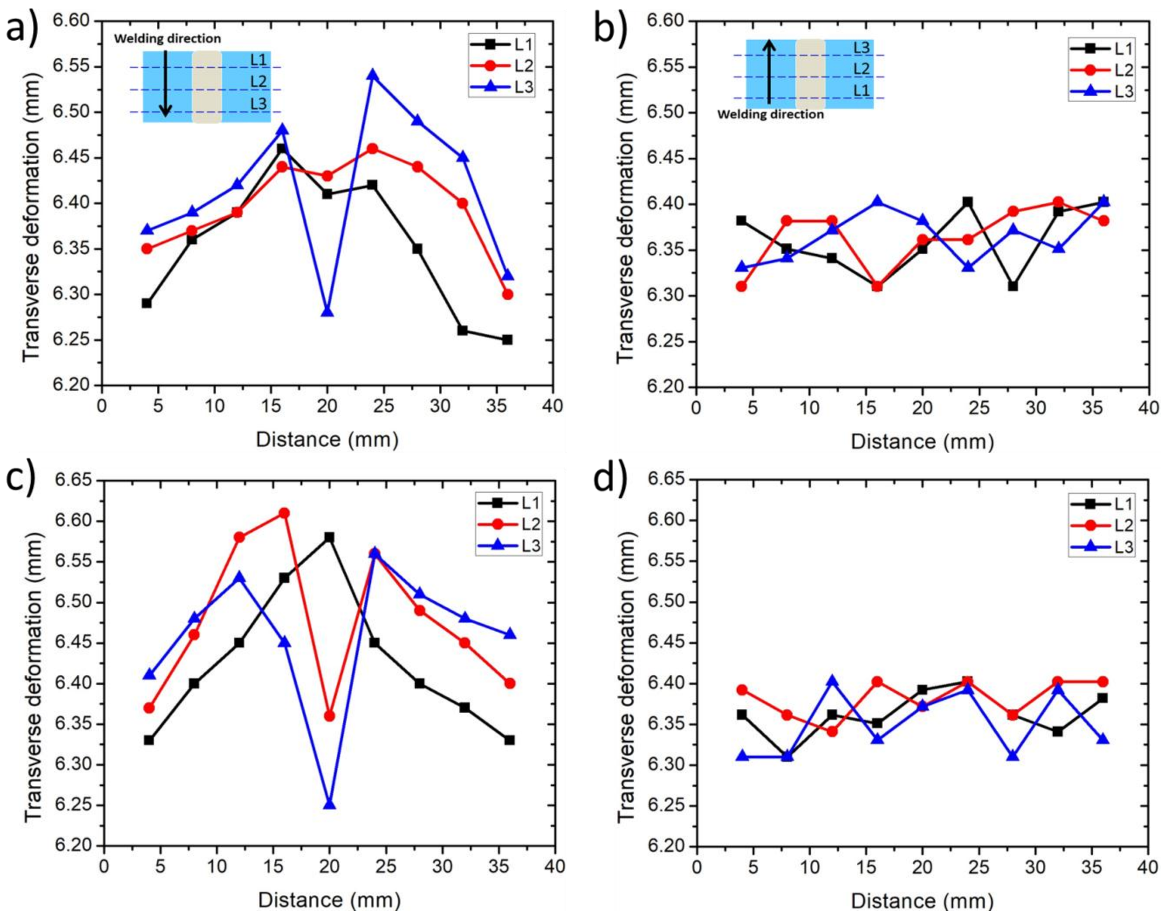

Figure 20. Post-welding transverse deformation distribution generated after the first and second passes in the TWIP-Ti steel weldments: a-b) 461 ~~J/mm~~, c-d) 565 ~~J/mm~~.

5. Conclusions

The following conclusions can be drawn from the experimental and numerical studies of the thermo-mechanical field in a pair of weldments performed in TWIP-Ti steel plates with low heat input:

1. The multilinear kinematic model with a strain rate of 0.01 s^{-1} was the average condition that accurately simulated residual stress and deformation distributions during the welding thermal cycle in the present TWIP-Ti steel.

2. The welding of the TWIP-Ti steel with the autogenous GTAW process in plate thickness ≥ 6.3 mm is feasible from the mechanical point of view (residual stress). In order to achieve this, a low heat input multi-pass welding process is necessary and a special preparation joint to maintain low heat affectation and residual stresses.

3.- The presence of remnant δ-ferrite in the FZ of TWIP-Ti steel joint affected the residual stress measurements producing high deviation in the XRD results. The lathy δ-ferrite was precipitated in the inter-dendritic.

4.- The residual stress critical zone (SCZ), the heterogeneous grain size distribution in the HAZ, and the lack of Mn and C segregation avoided the propagation of micro-cracks in both the FZ and the FZ-HAZ interface.

5.- The thermal diffusivity and thermal expansion coefficient affected residual stresses and plastic strain distributions in TWIP-Ti steel weldments. High heat concentration region gave rise to the SCZ.

6.- The joint preparation (double V-groove) allowed controlling the residual stress magnitude during the first weld pass. Meanwhile, the mechanical constraint produced a localized plastic strain zone.

Acknowledgments

This study is supported by the National Council on Science and Technology (Consejo Nacional de Ciencia y Tecnología-CONACYT-México) during the project CB-2012-01-0177572. The present research project was also supported by the Coordinación de la Investigación Científica-UMSNH (México) (CIC-1.8). V. García-García's studies were sponsored by the National Council on Science and Technology (Consejo Nacional de

Ciencia y Tecnología-México), N.B. 577720. J.M. Cabrera also thanks the financial funding from CONACYT to partially support his sabbatical leave at UMSNH.

References

[1] Roncery LM, Weber S, Theisen W. Welding of twinning-induced plasticity steels. Scripta Mater 2012; 66(12): 997-1001. https://doi.org/10.1016/j.scriptamat.2011.11.041

[2] Saha DC, Chang I, Park YD. Heat-affected zone liquation crack on resistance spot welded TWIP steels. Mater Charact 2014; 93: 40-51. https://doi.org/10.1016/j.matchar.2014.03.016

[3] Razmpoosh MH, Shamanian M, Esmailzadeh M. The microstructural evolution and mechanical properties of resistance spot welded Fe–31Mn–3Al–3Si TWIP steel. Mater Design 2015; 67: 571-576. https://doi.org/10.1016/j.matdes.2014.10.090

[4] Wang T, Zhang M, Xiong W, Liu R, Shi W, Li L. Microstructure and tensile properties of the laser welded TWIP steel and the deformation behavior of the fusion zone. Mater Design 2015; 83: 103-111. https://doi.org/10.1016/j.matdes.2015.06.002

[5] Spena PR, Rossini M, Cortese L, Matteis P, Scavino G, Firrao D. Laser welding between TWIP steels and automotive high-strength steels. In Characterization of Minerals, Metals, and Materials 2015; 13-20. Springer, Cham. https://doi.org/10.1007/978-3-319-48191-3_2

[6] Long H, Gery D, Carlier A, Maropoulos PG. Prediction of welding distortion in butt joint of thin plates. Mater Design 2009; 30(10): 4126-4135. https://doi.org/10.1016/j.matdes.2009.05.004

[7] D. Deng. FEM prediction of welding residual stress and distortion in carbon steel considering phase transformation effects. Mater Design 2009; 30: 359–366. https://doi.org/10.1016/j.matdes.2008.04.052

[8] Ishigami A, Roy MJ, Walsh JN, Withers PJ. The effect of the weld fusion zone shape on residual stress in submerged arc welding. Int J Adv Manuf Tech 2017; 90(9-12): 3451-3464. https://doi.org/10.1007/s00170-016-9542-z

[9] Zondi MC. Factors that affect welding-induced residual stress and distortions in pressure vessel steels and their mitigation techniques: a review. J Press Vess-T ASME 2014; 136(4): 040801. https://doi.org/10.1115/1.4026564

[10] Wei YH, Hou LF, Bin YAN. Microstructure and mechanical properties of TWIP steel joints. J Iron Steel Res Int 2014; 21(8): 749-756. https://doi.org/10.1016/S1006-706X(14)60137-0

[11] Yoo J, Kim B, Park Y, Lee C. Microstructural evolution and solidification cracking susceptibility of Fe–18Mn–0.6 C–xAl steel welds. J Mater Sci 2015; 50(1): 279-286. https://doi.org/10.1007/s10853-014-8586-4

[12] Mujica L, Weber S, Pinto H, Thomy C, Vollertsen F. Microstructure and mechanical properties of laser-welded joints of TWIP and TRIP steels. Mat Sci Eng A 2010; 527(7): 2071-2078. https://doi.org/10.1016/j.msea.2009.11.050

[13] Colombo TC, Rego RR, Otubo J, De Faria AR. Mechanical reliability of TWIP steel spot weldings. J Mater Process Tech 2019; 266: 662-674. https://doi.org/10.1016/j.jmatprotec.2018.11.021

[14] Shterner V, Molotnikov A, Timokhina I, Estrin Y, Beladi H. A constitutive model of the deformation behaviour of twinning induced plasticity (TWIP) steel at different temperatures. Mat Sci Eng A 2014; 613: 224-231. https://doi.org/10.1016/j.msea.2014.06.073

[15] Chin KG, Kang CY, Shin S, Hong S, Lee HS, Kim NJ. Effects of Al addition on deformation and fracture mechanisms in two high manganese TWIP steels. Mat Sci Eng A 2011; 528(6): 2922-2928. https://doi.org/10.1016/j.msea.2010.12.085

[16] Hong S, Shin SY, Kim HS, Lee S, Kim SK, Chin KG, Kim NJ. Effects of inclusions on delayed fracture properties of three twinning induced plasticity (TWIP) steels. Metall Mater Trans A 2013; 44(2): 776-786. https://doi.org/10.1007/s11661-012-1472-2

[17] Rossini NS, Dassisti M, Benyounis KY, Olabi AG. Methods of measuring residual stresses in components. Mater Design 2012; 35: 572-588. https://doi.org/10.1016/j.matdes.2011.08.022

[18] Withers PJ, Bhadeshia HKDH. Residual stress. Part 1–measurement techniques. Mater Sci Tech 2001; 17(4): 355-365. https://doi.org/10.1179/026708301101509980

[19] Chang PH, Teng TL. Numerical and experimental investigations on the residual stresses of the butt-welded joints. Comp Mater Sci 2004; 29(4): 511-522. https://doi.org/10.1016/j.commatsci.2003.12.005

[20] Lin J, Ma N, Lei Y, Murakawa H. Measurement of residual stress in arc welded lap joints by cosα X-ray diffraction method. J Mater Process Tech 2017; 243: 387-394. https://doi.org/10.1016/j.jmatprotec.2016.12.021

[21] Mousavi SA, Miresmaeili R. Experimental and numerical analyses of residual stress distributions in TIG welding process for 304L stainless steel. J Mater Process Tech 2008; 208(1-3): 383-394. https://doi.org/10.1016/j.jmatprotec.2008.01.015

[22] Li S, Ren S, Zhang Y, Deng D, Murakawa H. Numerical investigation of formation mechanism of welding residual stress in P92 steel multi-pass joints. J Mater Process Tech 2017; 244: 240-252. https://doi.org/10.1016/j.jmatprotec.2017.01.033

[23] Sattari-Far I, Farahani MR. Effect of the weld groove shape and pass number on residual stresses in butt-welded pipes. Int J Pres Ves Pip 2009; 86(11): 723-731. https://doi.org/10.1016/j.ijpvp.2009.07.007

[24] Rong Y, Huang Y, Zhang G, Mi G, Shao W. Laser beam welding of 316L T-joint: microstructure, microhardness, distortion, and residual stress. Int J Adv Manuf Tech 2017; 90(5-8): 2263-2270. https://doi.org/10.1007/s00170-016-9501-8

[25] Deng D, Murakawa H. Numerical simulation of temperature field and residual stress in multi-pass welds in stainless steel pipe and comparison with experimental measurements. Comp Mater Sci 2006; 37(3): 269-277. https://doi.org/10.1016/j.commatsci.2005.07.007

[26] Anca A, Cardona A, Risso J, Fachinotti VD. Finite element modeling of welding processes. Appl Math Model 2011; 35(2): 688-707. https://doi.org/10.1016/j.apm.2010.07.026

[27] Asserin O, Loredo A, Petelet M, Iooss B. Global sensitivity analysis in welding simulations What are the material data you really need? Finite Elem Anal Des 2011; 47(9): 1004-1016. https://doi.org/10.1016/j.finel.2011.03.016

[28] Deng D, Zhang C, Pu X, Liang W. Influence of material model on prediction accuracy of welding residual stress in an austenitic stainless steel multi-pass butt-welded joint.

J Mater Eng Perform 2017; 26(4): 1494-1505. https://doi.org/10.1007/s11665-017-2626-6

[29] Brickstad B, Josefson BL. A parametric study of residual stresses in multi-pass butt-welded stainless steel pipes. Int J Pres Ves Pip 1998; 75(1): 11-25. https://doi.org/10.1016/S0308-0161(97)00117-8

[30] Ueda Y, Murakawa H, Ma N. Welding deformation and residual stress prevention. USA: Butterworth-Heinemann; 2012.

[31] Zhu XK, Chao YJ. Effects of temperature-dependent material properties on welding simulation. Comput Struct 2002; 80(11): 967-976. https://doi.org/10.1016/S0045-7949(02)00040-8

[32] Ding-Quan Z, Jia-Wen H. Residual Stress Analysis by X-Ray Diffraction and Its Functions. China: Xi'an Jiaotong University Press Xi'an; 1999.

[33] ASTM, Standard Test Method for Knoop and Vickers Hardness of Materials, in ASTM Standard E384, 2011, ASTM International, West Conshohocken, PA http://dx.doi.org/10.1520/E0384-11E01.

[34] Lin J, Ma N, Lei Y, Murakawa H. Measurement of residual stress in arc welded lap joints by cosα X-ray diffraction method. J Mater Process Tech 2017; 243: 387-394. https://doi.org/10.1016/j.jmatprotec.2016.12.021

[35] Zhan K, Jiang CH, Ji V. Uniformity of residual stress distribution on the surface of S30432 austenitic stainless steel by different shot peening processes. Mater Lett 2013; 99: 61-64. https://doi.org/10.1016/j.matlet.2012.08.147

[36] Goldak J, Chakravarti A, Bibby M. A new finite element model for welding heat sources. Metall Mater Trans B 1984; 15: 299-305. https://doi.org/10.1007/BF02667333

[37] DuPont J.N, Marder A.R (1995) Thermal efficiency of arc welding processes. Weld J 74: 406-416.

[38] Bergman TL, Lavine AS, Incropera FP, DeWitt DP. Fundamentals of heat and mass transfer. USA: John Wiley & Sons; 2015.

[39] García-García V, Mejía I, Reyes-Calderón F. Comparative study on weldability of Ti-containing TWIP and AISI 304L austenitic steels through the autogenous-GTAW

process. Int J Ad Manuf Tech 2018; 98(9-12): 2365-2376. https://doi.org/10.1007/s00170-018-2392-0

[40] Liang W, Murakawa H, Deng D. Investigation of welding residual stress distribution in a thick-plate joint with an emphasis on the features near weld end-start. Mater Design 2015; 67: 303-312. https://doi.org/10.1016/j.matdes.2014.11.037

[41] Lemaitre J, Chaboche JL. Mechanics of solid materials. UK: Cambridge university press; 1994.

[42] Jung JE, Park J, Kim JS, Jeon JB, Kim SK, Chang YW. Temperature effect on twin formation kinetics and deformation behavior of Fe-18Mn-0.6 C TWIP steel. Met Mater Int 2014; 20(1): 27-34. https://doi.org/10.1007/s12540-014-1008-y

[43] Hamada AS, Karjalainen LP. Hot ductility behaviour of high-Mn TWIP steels. Mat Sci Eng A 2011; 528(3): 1819-1827. https://doi.org/10.1016/j.msea.2010.11.030

[44] Curtze S, Kuokkala VT. Dependence of tensile deformation behavior of TWIP steels on stacking fault energy, temperature and strain rate. Acta Mater 2010; 58(15): 5129-5141. https://doi.org/10.1016/j.actamat.2010.05.049

[45] Madivala M, Schwedt A, Wong SL, Roters F, Prahl U, Bleck W. Temperature dependent strain hardening and fracture behavior of TWIP steel. Int J Plasticity 2018; 104: 80-103. https://doi.org/10.1016/j.ijplas.2018.02.001

[46] ANSYS Inc. ANSYS Mechanical User´s Guide. ANSYS Inc, USA: 2018.

[47] Muránsky O, Hamelin CJ, Smith MC, Bendeich PJ, Edwards L. The effect of plasticity theory on predicted residual stress fields in numerical weld analyses. Comp Mater Sci 2012; 54: 125-134. https://doi.org/10.1016/j.commatsci.2011.10.026

[48] Deng D, Murakawa H. Numerical simulation of temperature field and residual stress in multi-pass welds in stainless steel pipe and comparison with experimental measurements. Comp Mater Sci 2006; 37(3): 269-277. https://doi.org/10.1016/j.commatsci.2005.07.007

[49] Hong S, Lee J, Lee BJ, Kim HS, Kim SK, Chin KG, Lee S. Effects of intergranular carbide precipitation on delayed fracture behavior in three TWinning Induced Plasticity (TWIP) steels. Mat Sci Eng A 2013; 587: 85-99. https://doi.org/10.1016/j.msea.2013.08.063

[50] Aloraier AS, Joshi S. Residual stresses in flux cored arc welding process in bead-on-plate specimens. Mat Sci Eng A 2012; 534: 13-21. https://doi.org/10.1016/j.msea.2011.10.107

[51] Heinze C, Schwenk C, Rethmeier M. Numerical calculation of residual stress development of multi-pass gas metal arc welding. J Constr Steel Res 2012; 72: 12-19. https://doi.org/10.1016/j.jcsr.2011.08.011

[52] García-García V, Mejía I, Reyes-Calderón F. Experimental and FEM study of Ti-containing TWIP steel weldability. J Mater Process Tech 2018; 261: 107-122. https://doi.org/10.1016/j.jmatprotec.2018.05.028

[53] Teng TL, Chang PH, Tseng WC. Effect of welding sequences on residual stresses. Comput Struct 2003; 81(5): 273-286. https://doi.org/10.1016/S0045-7949(02)00447-9

[54] Lemos GVB, Cunha PHCP, Nunes RM, Bergmann L, Dos Santos JF, Clarke T. Residual stress and microstructural features of friction-stir-welded GL E36 shipbuilding steel. Mater Sci Tech 2018; 34(1): 95-103. https://doi.org/10.1080/02670836.2017.1361148

[55] Rae W, Lomas Z, Jackson M, Rahimi S. Measurements of residual stress and microstructural evolution in electron beam welded Ti-6Al-4V using multiple techniques. Mater Charact 2017; 132: 10-19. https://doi.org/10.1016/j.matchar.2017.07.042

[56] Teng TL, Lin CC. Effect of welding conditions on residual stresses due to butt welds. Int J Pres Ves Pip 1998; 75(12): 857-864. https://doi.org/10.1016/S0308-0161(98)00084-2

[57] Khandkar MZH, Khan JA, Reynolds AP, Sutton MA. Predicting residual thermal stresses in friction stir welded metals. J Mater Process Tech 2006; 174(1-3): 195-203. https://doi.org/10.1016/j.jmatprotec.2005.12.013

Table captions:

Table 1. Autogenous GTAW process parameters used in the TWIP-Ti weldments.

Table 2. Tensile and compressive residual stresses estimated by the isotropic and kinematic hardening models at different strain rates.

Figure captions:

Figure 1. Set up for the GTAW process applied in the TWIP-Ti steel weld samples of 6.3 mm plate thickness.

Figure 2. Set up for the post-welding transverse deformation measurement.

Figure 3. TWIP-Ti steel mechanical properties temperature dependent calculated by means of the JMatPro® 9.1: a) Young's modulus, b) Tangent modulus, c) Thermal expansion coefficient, d) Poisson ratio.

Figure 4. Engineering stress-strain curves of TWIP-Ti steel at different temperatures and strain rates of: a) 0.001 s^{-1}, b) 0.01 s^{-1}, c) 0.1 s^{-1}, d) 1 s^{-1}, e) 10 s^{-1} and f) 100 s^{-1}.

Figure 5. Validation of engineering stress-strain curves estimated through JMatPro® 9.1 software with tensile tests experimental data carried out at a strain rate of ~~0.001s^{-1}~~ and different temperatures: a) ~~300°C~~ b) ~~400°C~~ c) ~~600°C~~ d) ~~700°C~~ e) ~~800°C~~.

Figure 6. a) Bilinear stress-strain relationship, b) Multilinear stress-strain relationship.

Figure 7. a) Tack welds applied in corners of TWIP-Ti steel plates, b) Essential boundary conditions applied into the calculation domain.

Figure 8. a) Mesh used in the welding thermal and mechanical models, b) Mesh elements orthogonal quality distribution, c) Mesh elements skewness distribution, d) Mesh-independent solution study in the thermal model.

Figure 9. Longitudinal residual stress estimated at different strain rates by different hardening models: a) Bilinear isotropic, b) Multilinear isotropic, c) Bilinear kinematic, d) Multilinear kinematic.

Figure 10. Residual stress estimated numerically vs X-ray diffraction measurements ($\sin^2 \psi$ method) for welded joint 1.

Figure 11. Diffraction peak ($2\theta = 89.7°$) analyzed for residual stress measurements in FZ.

Figure 12. Diffraction profiles obtained from: a) BM, b) FZ.

Figure 13. Longitudinal residual stress transient distribution estimated by the FE thermo-mechanical model (multilinear kinematic hardening model) in TWIP-Ti steel weldment 1 (461 ~~J/mm~~): a) 10 s, b) ~~25s~~, c) 70 s, d) 600 s.

Figure 14. Longitudinal residual stress transient distribution estimated by the FE thermo-mechanical model (multilinear kinematic hardening model) in TWIP-Ti steel weldment 2 (565 ~~J/mm~~): a) 10 s, b) ~~25s~~, c) 70 s, d) 600 s.

Figure 15. Post-welding transverse residual stress distribution (first pass) estimated in the upper and lower faces of TWIP-Ti steel weldments: a) 461 ~~J/mm~~, b) 565 ~~J/mm~~.

Figure 16. Microhardness profiles: a) weldment 1 (461 ~~J/mm~~), b) weldment 2 (565 ~~J/mm~~), c) Transverse residual stress distribution in the mid-plane of the TWIP-Ti weldment of low heat input (461 ~~J/mm~~).

Figure 17. 2-D contours of temperature distribution, thermal conductivity and thermal expansion coefficient in TWIP-Ti steel weldments: a) 565 ~~J/mm~~, b) 461 ~~J/mm~~.

Figure 18. Microstructural observations of the TWIP-Ti weldment 1: a) FZ-center, b) FZ-HAZ interface, c) Remnant δ-ferrite found in FZ boundary (weldment 1).

Figure 19. Welding plastic strain transient distribution estimated by the FE thermo-mechanical model (with multilinear kinematic hardening model) in TWIP-Ti steel weldment 1 (461 ~~J/mm~~) at: a) 10 s, b) 25 s, c) 70 s, d) 600 s.

Figure 20. Post-welding transverse deformation distribution generated after the first and second passes in the TWIP-Ti steel weldments: a-b) 461 ~~J/mm~~, c-d) 565 ~~J/mm~~.